A Model of the Wind-Driven Seasonal Variability in the Tropical North Pacific, with Validation through Altimeter Data

STEFANO PIERINI*

Dipartimento di Fisica, Università dell'Aquila, Coppito, Italy

(Manuscript received 6 March 2002, in final form 21 March 2003)

ABSTRACT

The wind-driven seasonal variability in the tropical North Pacific Ocean is analyzed by means of a two-layer primitive equation ocean model implemented in an idealized Pacific extending from 30°S to 52°N and forced by an analytic seasonally varying wind stress field derived from ECMWF winds. The oceanic response in the tropical region is found to be mainly in the form of annual beta-refracted baroclinic Rossby waves radiating from the eastern boundary. Validation of these results with TOPEX/Poseidon (T/P) altimeter data is carried out. Zonal longitude–time diagrams of sea surface height anomalies and zonally integrated meridional transports computed from T/P data and from the winds through the Sverdrup relation by Stammer are compared with the corresponding quantities obtained from the model results. Such comparison shows that the model does capture the essential features of the wind-driven seasonal variability in the tropical North Pacific. The analysis of the model results, based also on sensitivity experiments, shows that the waves radiating from the eastern boundary are generated by the passage of northward-propagating coastal Kelvin waves, which are in turn produced remotely by seasonally varying winds in the equatorial wave guide, through a dynamical mechanism known to play a major role in the dynamics of El Niño events. Therefore, these model results suggest that the annual Rossby waves observed in the eastern tropical North Pacific may be mainly generated remotely in the equatorial band rather than by varying winds along the eastern coast, as considered in other studies.

1. Introduction

The main periodicity in the large-scale ocean heat content and circulation is the seasonal cycle, because of annual variations of heat, freshwater, and momentum exchanges with the atmosphere. In particular, the seasonal variability of the large-scale ocean circulation is mainly driven by the momentum flux associated with the wind and has very different features for different latitudinal bands. At mid- and high latitudes the oceanic response to seasonally varying winds is mainly barotropic and is driven by the Ekman pumping (e.g., Pedlosky 1996), which is proportional to the local wind stress curl. Baroclinic Rossby waves give a small contribution for latitudes higher than the critical one for the annual period ($\varphi \sim 35°$). On the other hand, in the Tropics annual baroclinic Rossby waves, being much faster than those at midlatitudes, are able to shape the wind-driven seasonal variability in the central and eastern tropical Pacific and Atlantic Oceans (e.g., White 1977; Meyers 1979; White and Saur 1981; Krauss and Wuebber 1982; Cummins et al. 1986; Herrmann and Kraus, 1989). Still in the Tropics, in the central and western part of the basins, Ekman pumping and topographic interactions can give important contributions to the seasonal variability.

Experimental investigations through in situ measurements put in evidence important aspects of the seasonal variability, but the monitoring of the latter on a global scale was possible only after the advent of remote sensing. Satellite altimetry (e.g., Robinson 1994; Fu and Cazenave 2001) and, in particular, the most recent U.S./French TOPEX/Poseidon (T/P) and European *ERS-1/2* missions have provided a revolutionizing tool to study seasonal changes in both the upper-ocean heat storage and the large-scale circulation over the global ocean. The not (yet) sufficiently accurate knowledge of the geoid has, up to now, limited the application of altimeter data to the study of the fluctuating part of the sea surface height (SSH) signal, but this is perfectly compatible with the analysis of the oceanic variability. After filtering out the tidal, inverted barometer and steric height

* Current affiliation: Istituto di Meteorologia e Oceanografia, Università di Napoli ''Parthenope,'' Naples, Italy.

Corresponding author address: Stefano Pierini, Istituto di Meteorologia e Oceanografia, Università di Napoli ''Parthenope,'' Via A. De Gasperi, 5, 80133 Naples, Italy.
E-mail: stefano.pierini@uninav.it

signals, the remaining residual is a basically wind-driven ''dynamically active'' SSH anomaly from which geostrophic surface current fluctuations can be computed. Many studies have been carried out in which both the observational evidence of the seasonal variability and its physical interpretation were based on altimeter data [e.g., see Fu and Chelton (2001) and Picaut and Busalacchi (2001) for a review].

The most striking (and energetic) aspect of the wind-driven seasonal variability in the eastern tropical Pacific (and for very low latitudes also in the central part of the ocean) is the presence of annual baroclinic Rossby waves radiating from the eastern boundary and yielding a pronounced ''beta'' refraction toward the equator due to the dependence of phase speed with latitude. Although this was first recognized through the analysis of in situ data (e.g., White 1977; Meyers 1979; Kessler 1990), it was only with altimeter data that this prominent seasonal feature could be analyzed synoptically (e.g., Chelton and Schlax 1996). According to a fairly common opinion such waves (and their Atlantic counterpart) are thought to be generated at the oceanic eastern boundary mainly by the local action of seasonally varying winds (e.g., White 1977; Meyers 1979; White and Saur 1981; Krauss and Wuebber 1982; Cummins et al. 1986; Herrmann and Krauss 1989). However, it is interesting to notice that wave energy in the eastern Pacific, as observed in T/P data, was found to be strongly correlated with SSH anomalies at the equator (Vivier et al. 1999), suggesting a predominantly nonlocal generating mechanism. The latter is presumably due to Rossby wave forcing from poleward propagating coastal Kelvin waves generated in the equatorial region by wind stress anomalies through a teleconnection proposed by McCreary (1976) in the different context of El Niño dynamics. So the following questions arise: are the annual Rossby waves radiating from the eastern boundary of the North Pacific Ocean generated at the coast mainly through a local or a remote forcing mechanism? Moreover, in the case of a prevalent remote generation, is the teleconnection cited above the actual physical mechanism that shapes the response?

The main aim of the present paper is to provide possible answers to these questions. A process-oriented model study of the wind-driven seasonal variability in the North Pacific Ocean was therefore carried out, along with validation through T/P altimeter data. The model results have supported the hypothesis of a predominant remote forcing mechanism; therefore sensitivity experiments have also been performed in order to shed further insight into its functioning.

The paper is organized as follows. In section 2 the mathematical model and the wind forcing used are discussed. A two-layer primitive equation ocean model is implemented in an idealized Pacific spanning the latitudinal range $\varphi = 30°\text{S}–52°\text{N}$. The forcing is provided by an idealized seasonally varying wind field obtained from the European Centre for Medium-Range Weather Forecasts (ECMWF) seasonal climatology (Rienecker et al. 1996). In section 3 the analysis of the model results is presented. Annual baroclinic Rossby waves radiating from the eastern boundary are identified, and the typical beta-refraction patterns due to the variation of wave speed with latitude are recognized. A first evidence is then provided that such Rossby waves are generated by the passage of northward-propagating coastal Kelvin waves originating from the equatorial band. In section 4 validation with Stammer's (1997) altimeter data is carried out. Zonal x–t diagrams of sea surface height anomalies and zonally integrated meridional transports computed from T/P data and from the winds through the Sverdrup relation are compared with the corresponding quantities obtained from the model results: such comparison shows that the model does capture the essential features of the wind-driven seasonal variability in the tropical North Pacific. It is also shown that the time-dependent Sverdrup balance holds in the tropical ocean, although it is masked in the SSH signal by the overwhelming contribution of the baroclinic Rossby wave dynamics. In section 5 sensitivity experiments are presented with the aim of better understanding the process through which annual Rossby waves are generated at the eastern boundary. First, the model is forced by the same wind field used in the basic run, but in which variations of the phase in the equatorial band are introduced; second, a wind field confined in the equatorial band is considered. The general conclusion is that ageostrophic boundary effects rather than the local Ekman pumping generate the wind-driven seasonal variability in the eastern and central tropical North Pacific. Moreover, the eastern boundary radiation of annual Rossby waves is attributed to the same dynamical mechanism known to act in El Niño events.

2. The model

a. The mathematical model

In view of the process-oriented nature of this study it appears desirable not to use a fully realistic three-dimensional ocean general circulation model (whose complexity could overshadow the dynamical mechanisms to be analyzed) but rather a simplified model, which, however, must include the main effects related to the wind-driven oceanic variability. Moreover, the free surface should also be included because it would allow simulation of the altimeter signal with which comparison is made. In this framework a two-layer, shallow water, flat bottom, nonlinear primitive equation ocean model with free surface is used. The equations for the upper and lower layer, respectively, are given below (see Fig. 1):

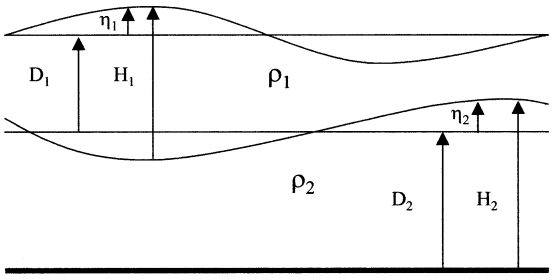

FIG. 1. The two-layer shallow water model setup.

$$u_{1t} + u_1 u_{1x} + v_1 u_{1y} - f v_1 = -g\eta_{1x} + \frac{\tau_x}{\rho_1 H_1} + A_H \nabla^2 u_1$$

$$v_{1t} + u_1 v_{1x} + v_1 v_{1y} + f u_1 = -g\eta_{1y} + \frac{\tau_y}{\rho_1 H_1} + A_H \nabla^2 v_1$$

$$H_{1t} + (H_1 u_1)_x + (H_1 v_1)_y = 0, \quad (1)$$

$$u_{2t} + u_2 u_{2x} + v_2 u_{2y} - f v_2 = -\alpha\eta_{1x} - g'\eta_{2x} + A_H \nabla^2 u_2$$

$$v_{2t} + u_2 v_{2x} + v_2 v_{2y} + f u_2 = -\alpha\eta_{1y} - g'\eta_{2y} + A_H \nabla^2 v_2$$

$$H_{2t} + (H_2 u_2)_x + (H_2 v_2)_y = 0, \quad (2)$$

where $\alpha = g\rho_1/\rho_2$, $g' = g(\rho_2 - \rho_1)/\overline{\rho}$, $\mathbf{u}_i = (u_i, v_i)$, and ρ_i ($i = 1, 2$) are the upper- and lower-layer horizontal velocities and densities, respectively; η_1 and η_2 are the sea surface and interface displacement, respectively; g is the acceleration of gravity; A_H is the lateral eddy viscosity coefficient; and $\boldsymbol{\tau}$ is the surface wind stress. The following parameter values have been chosen: $D_1 = 200$ m, $D_2 = 3800$ m, $\rho_1 = 1.026$ g cm^{-3}, $\rho_2 = 1.028$ g cm^{-3}, $A_H = 5000$ m^2 s^{-1}. The spatial and temporal steps are $\Delta x = 100$ km, $\Delta y = 111$ km (so that 1 grid step corresponds to 1° in latitude) and $\Delta t = 130$ s. Free-slip boundary conditions are imposed along the closed contour lines and integration is carried out starting from the state at rest.

This model is the two-layer extension of a barotropic wind-driven model developed for a process-oriented regional ocean study (Pierini 1996). The equations are solved through an explicit leapfrog finite-difference scheme on the Arakawa C grid. The integration domain is a rectangle of zonal width $L = 9000$ km spanning the latitudinal range $\varphi = 30°$S–52°N (L is chosen as a rough meridional mean value of the zonal width, and sensitivity experiments not shown insure that the model results are virtually independent on the choice of L, provided that it is sufficiently large). Along y the Coriolis parameter $f = 2\Omega_{\text{earth}} \sin\varphi$ models correctly the Coriolis force at different latitudes. Although we are interested in the North Pacific, the domain of integration has been chosen to include also a southern sector in order to avoid unrealistic effects associated with a rigid boundary located at the equator.

In many cases a reduced-gravity model is used to study the upper-ocean dynamics. It has the computational advantage of allowing for a Δt much larger than that required for a free-surface model solved through an explicit algorithm (such as the one adopted in this study). In addition, the free surface could be computed from the thermocline displacement at low latitudes because, there, the former mirrors the latter through the factor $\Delta\rho/\rho$. However, this does not hold at midlatitudes, where the wind-driven seasonal variability is mainly barotropic. Therefore, if a process study on the wind-driven variability is to be performed with application to altimeter data, then the use of a model with free surface is essential. A further reason for using a model with only active layers lies in the possibility of computing a depth-averaged transport, which can then be compared with the Sverdrup transport, as done in section 4b.

b. The wind forcing

In line with the relatively idealized mathematical model an analytic wind stress was chosen, whose structure does, however, include the main aspects of the wind seasonal variability over the North Pacific Ocean. The seasonal signal for the wind stress curl in the North Pacific was calculated by Rienecker and Ehret (1988) from the Comprehensive Ocean–Atmosphere Data Set (COADS). It can be schematized by three zonal belts: $\varphi \approx 0°$–10°N, $\varphi \approx 10°$–30°/40°N (the northern boundary being at $\varphi \approx 30°$ at the western side and at $\varphi \approx 40°$ at the eastern side), and $\varphi \approx 30°/40°$–55°N. There is a phase change of 4 months at $\varphi \approx 10°$N, while a phase change of 6 months is found at the midlatitude boundary (in other words, the signal in the intermediate belt and that in the northern belt are opposite in phase). Isoguchi et al. (1997) computed empirical orthogonal functions (EOFs) of surface wind stress curl ECMWF fields in the mid- and high-latitude North Pacific: the first EOF, having a mainly seasonal variation, represents a north–south oscillation with a nodal axis at around 35°N, in agreement with Rienecker and Ehret (1988). Also using ECMWF surface winds, White et al. (1998) presented a root-mean-square (rms) map of the wind stress curl anomalies that, once more, confirms the existence of two main lobes for the seasonal variability of the surface wind stress curl over the North Pacific divided at approximately $\varphi \approx 35°$N, with the northern lobe (representing the seasonal variability of the Aleutian low) having an amplitude that is about 1.5 times that of the southern one.

Rienecker et al. (1996) have carried out a comparison of different surface wind products over the North Pacific Ocean, and have provided profiles of the seasonal zonally averaged zonal component of wind stress as a function of latitude, derived from various wind stress estimates from July 1987 to December 1989. In Fig. 2 the winter (averaged over December, January, and February, line DJF) and summer (averaged over June, July, and August, line JJA) meridional profiles of the 10-m

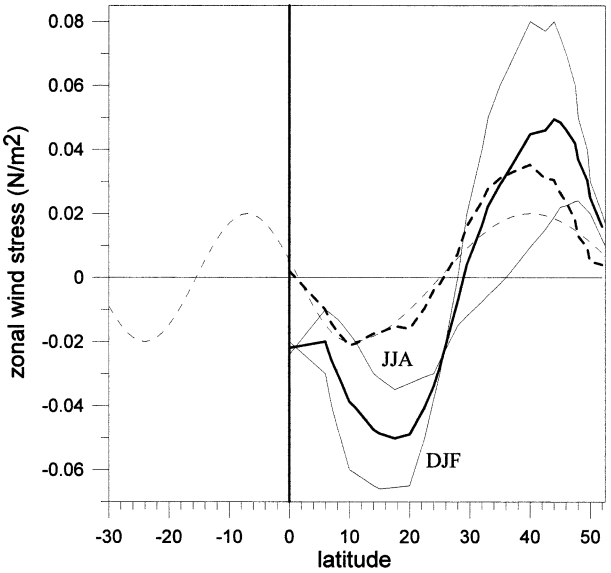

FIG. 2. Thin solid lines: meridional profiles of the 10-m ECMWF zonally averaged zonal wind stress over the North Pacific Ocean averaged over Dec–Jan–Feb (line DJF) and Jun–Jul–Aug (line JJA), as digitized from Fig. 5 of Rienecker et al. (1996). Thick solid line: meriodional profile of the annual mean obtained by averaging the DJF and JJA profiles. Thick dashed line: meridional profile of the seasonally varying winds (see text). Thin dashed line: analytical approximation of the thick dashed line representing the meridional profile of the seasonally varying zonal wind stress (at $x = 4500$ km) used to force the circulation model.

ECMWF zonal wind stress analysis as digitized from Fig. 5 of Rienecker et al. (1996) are reported. The wind stress field used in the present paper is based on this information. First of all an annual mean can be obtained by averaging the preceding two profiles (thick solid line of Fig. 2). A seasonally variable stress can then be derived: the thick dashed line of Fig. 2 gives the amplitude of the seasonally varying wind that, superimposed on the annual mean, allows passage from the line DJF to (6 months later) the line JJA. Such profile is then approximated by the thin dashed line, which is composed of two sinusoidal functions of different amplitudes and wavenumbers matched at $\varphi = 10°$. The analytical function approximates very well the observational profile from $\varphi = 0°$ to $\varphi \approx 25°$, which is the region of our interest. For higher latitudes the analytical signal underestimates the experimental signal by $\approx$50%, but we do not expect this to affect the oceanic response in the tropical region. For negative latitudes the signal is simply the extension of the low-latitude ($\varphi < 10°$) sinusoid. While for latitudes between $-10°$ and the equator the signal can be considered as approximating fairly well the actual seasonal variability, for smaller negative values larger departures can be expected. However, the role of buffer zone played by the integration domain for negative latitudes makes this departure irrelevant for the oceanic response in the northern tropical region.

A two-dimensional zonal wind stress field $\tau_0(x, y)$ is then constructed (Fig. 3a) by imposing a meridional profile at $x = L/2$ ($=4500$ km) equal to the analytical profile just obtained (thin dashed line of Fig. 2), and a zonal sinusoidal modulation. The corresponding wind stress curl field is shown in Fig. 3b. The two almost opposite-in-phase lobes divided at $\varphi = 10°$ discussed at the beginning of this subsection are present; a northern lobe, opposite in phase with respect to the midlatitude one, is also present above $\varphi = 40°$. In conclusion, the time-dependent zonal wind stress used to force the circulation model was chosen as

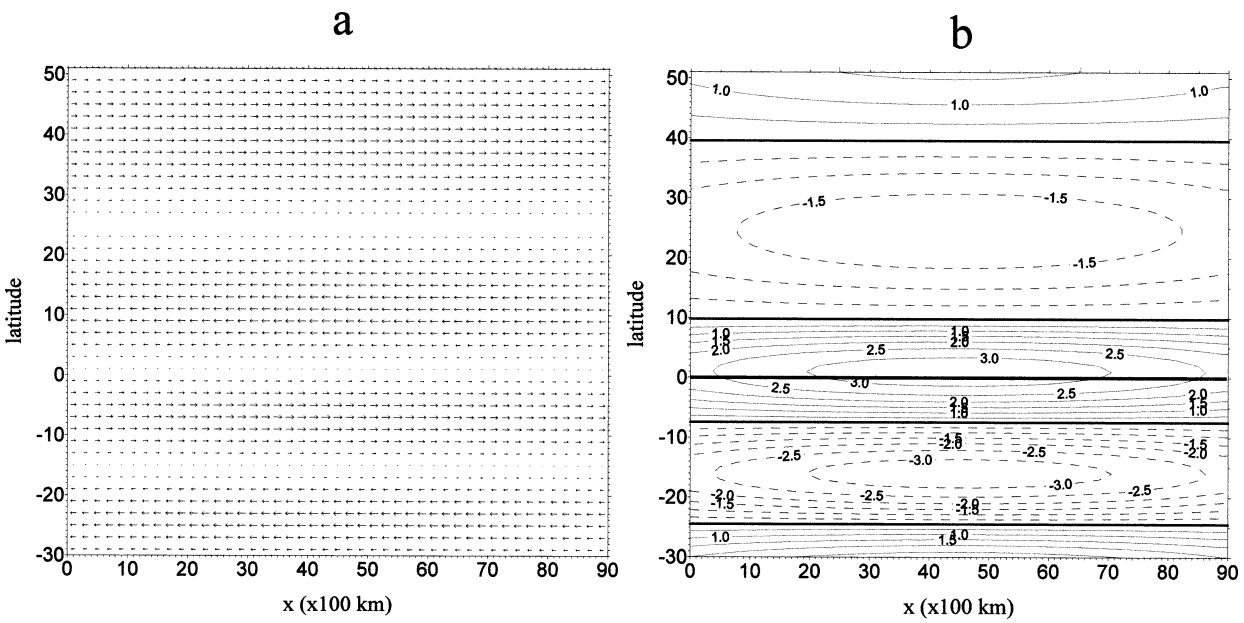

FIG. 3. (a) Map of $\tau_0(x, y)$ (for the units, refer to the thin dashed line of Fig. 2) and (b) map of $\text{curl}_z\ \tau_0$ (amplitudes: 10^{-8} N m^{-3}).

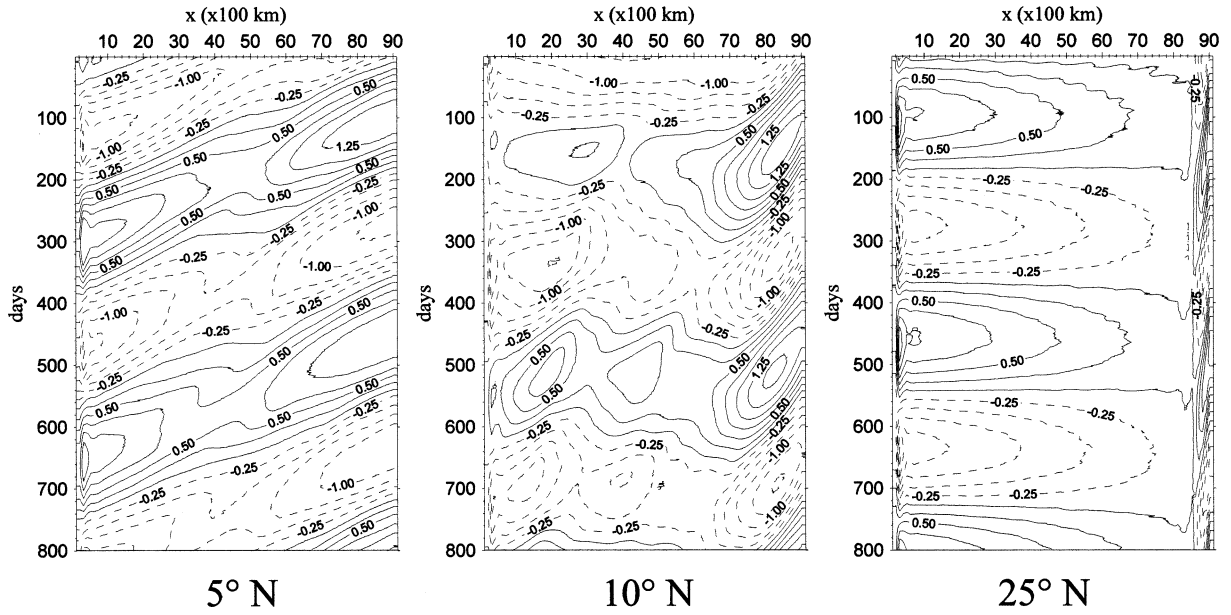

FIG. 4. SSH x–t diagrams at $\varphi = 5°$, 10°, and 25°N (amplitudes: cm). These diagrams are directly comparable with those of Plate 3 of Stammer (1997).

$$\tau(x, y, t) = \tau_0(x, y) \sin(\omega t), \tag{3}$$

where $\omega = 2\pi/T$, $T = 360$ days, and the meridional profile τ_0 ($x = 4500$ km, y) is given by the thin dashed line of Fig. 2. From what was said earlier in this section and from (3) it derives that the midwinter condition (line DJF, which can be identified roughly with 15 January) corresponds to $t = 90 + 360k$ days ($k = 0, 1, 2, \ldots$), while the midsummer condition (line JJA, which can be identified roughly with 15 July) corresponds to $t = 270 + 360k$ days.

Although the most salient features of the North Pacific seasonally variable wind stress are reproduced by (3), some simplifications deserve to be emphasized. For spatial variation, the zonally symmetric wind field $\tau_0(x, y)$ does not reproduce the observed east–west asymmetry of the wind stress curl, particularly evident at $\varphi > 30°$, but this may not be considered a major drawback in a process-oriented study of the tropical Pacific. For temporal variation of the wind stress, connecting the DJF and JJA profiles through a monochromatic sinusoidal temporal variation neglects the presence of higher harmonics that can distort the actual seasonal time dependence; moreover, the correspondence of 15 January with $t = 90 + 360k$ days and 15 July with $t = 270 + 360k$ days contains also some degree of arbitrariness because the signal is not symmetrically distributed during the seasons. However these choices are in line with the present process-oriented approach.

A more serious simplification concerns the fact that while, as reported by Rienecker and Ehret (1988), near 10°N there is a phase change of 4 months, in (3) the phase change is 6 months. In principle this 2-month phase difference could be reproduced in the analytical form of τ_0, but this would require introducing parameters whose values could only be determined by consideration of the original ECMWF wind data. However, doing that would be in contrast with the simplified nature of our analysis. Another important reason for accepting this discrepancy is that, as is evident in the following sections, most of the seasonal variability in the eastern and central tropical Pacific is determined by the wind in a narrow near-equatorial band, so that a corrected oceanic response outside such band can be obtained by simply shifting the response by 2 months. We will consider this point again in the validation with altimeter data in section 4b.

3. Analysis of the response

In this section we analyze the oceanic response to wind forcing in (3) with $\tau_0(x, y)$ shown in Fig. 3a (with profile at $x = L/2$ shown by the thin dashed line of Fig. 2). The initial time of integration is chosen at $t = -180$ days, so that time $t = 0$ (corresponding roughly to 15 October) is preceded by a spinup period of 6 months. Figures 4 and 5 show the x–t diagrams of the sea surface height (SSH) η_1 and interface displacement η_2, respectively, along zonal sections at $\varphi = 5°$, 10°, and 25°N. The signatures provide a clear indication that Rossby waves are emanating from the eastern boundary, extending over a limited zonal region whose width decreases with increasing latitude. The inclination of the isolines is associated with westward propagation; moreover, the fact that the SSH and interface displacement at $\varphi = 5°$ and 10°N (and at $\varphi = 25°$N in the western part of the basin) are opposite in phase and with am-

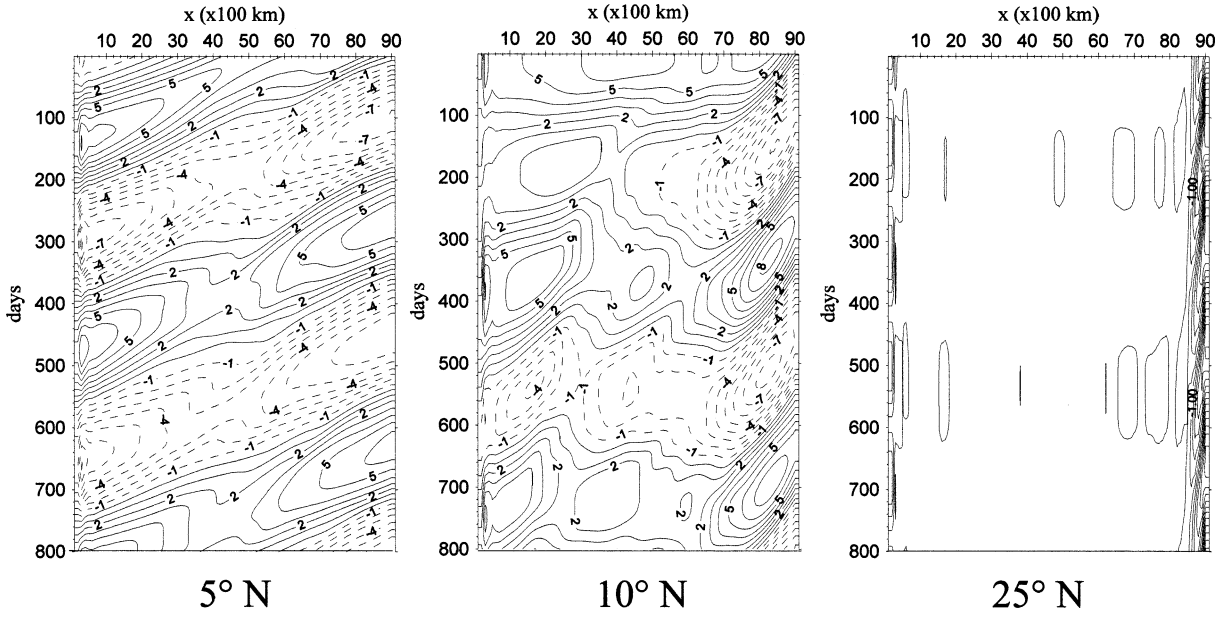

FIG. 5. As in Fig. 4 but of interface displacement at $\varphi = 5°$N, 10°N, and 25°N (amplitudes in m).

plitudes whose ratio is $\approx \Delta\rho/\rho$, indicates that first-mode (the only one admitted in a two-layer model) annual baroclinic Rossby waves are present. In contrast to the large baroclinic signal at low latitudes, a mainly barotropic response is found at $\varphi = 25°$N west of $x \sim 8000$ km, where the large time-dependent westward-intensified signal present in the SSH west of ≈1000 km from the eastern coast is absent in the interface displacement [this could be expected in advance on the basis of general arguments concerning the oceanic seasonal variability, since the latter is mainly barotropic for latitudes higher than ~20°, as recognized by Gill and Niiler (1973)]. In the following sections we will consider the cause of the different penetration of Rossby waves emanating from the eastern boundary (section 3a) and the origin of such waves from the equatorial wave guide (section 3b)

a. Beta refraction

In Fig. 6 a snapshot of the SSH (Fig. 6a) and interface displacement (Fig. 6b) at $t = 630$ days (≈15 July) are

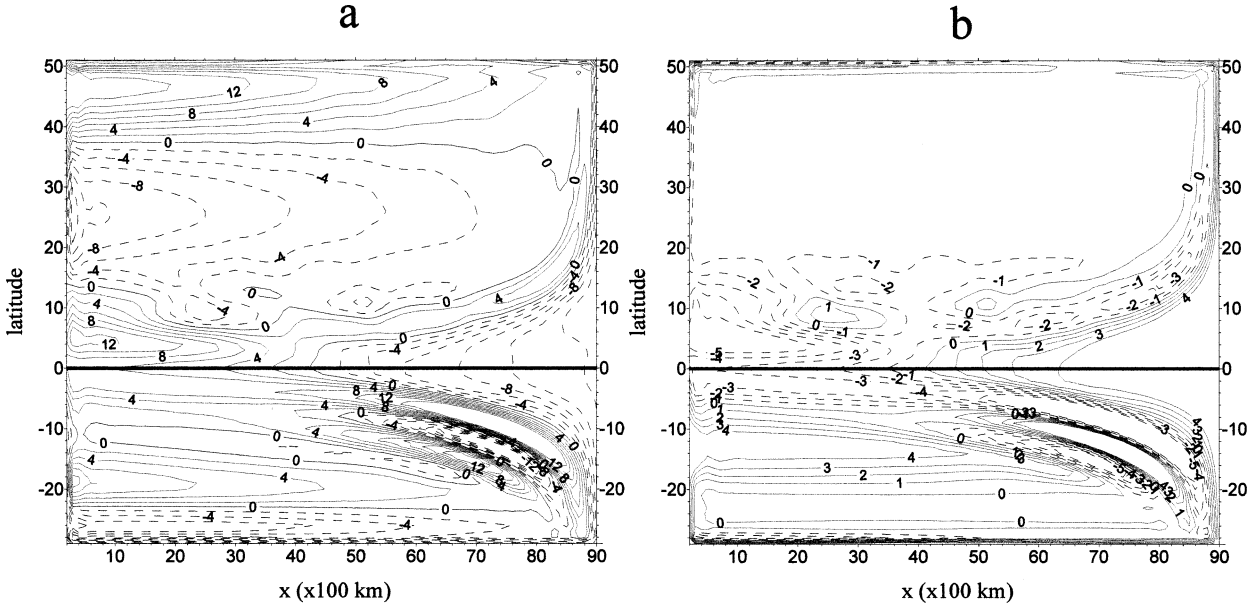

FIG. 6. (a) Snapshots of the SSH (cm) and (b) of the interface displacement (m) at $t = 630$ days.

shown. The most prominent feature evident in the flow patterns in the intertropical region is a strongly latitude-dependent shadow zone in which Rossby waves cannot penetrate, and whose existence is due to the so-called beta refraction (e.g., White 1977; Schopf et al. 1981; Philander 1990). From Fig. 6 one can note that near the eastern boundary the crests and troughs yield an almost north–south alignment (vanishing meridional wave number k_y). However, after having left the eastern boundary propagating westward, a wave packet would be refracted toward the equator (with k_y tending to be much larger than k_x), because only in this way can the wave frequency remain invariant under the constraint given by the dispersion relation for Rossby waves. Another way of interpreting the beta-refraction signature is by observing [as did Philander and Yoon (1982) for waves generated by fluctuating alongshore winds, but the present case is basically equivalent] that the offshore scale of the response is the internal Rossby radius of deformation R_i [$R_i = \sqrt{g'\overline{D}}/f$, $\overline{D} = D_1D_2/(D_1 + D_2)$] for forcing frequencies higher than the Rossby cutoff frequency $\overline{\omega} = -\beta R_i/2$ (the maximum frequency for which Rossby waves can exist) while, for lower forcing frequencies, it is equal to the distance covered by a Rossby wave during a period. It is easy to check that our numerical simulation verifies this property. Indeed, for latitudes lower than 36°N (where the cutoff period is 1 yr), the westernmost isoline of both SSH and interface displacement in Figs. 4 and 5 is located at a distance from the eastern boundary about equal to $l = c_gT$, ($T = 360$ days) where the zonal component of the group velocity c_g (nearly equal to the phase velocity because, at such low latitudes, baroclinic Rossby waves are virtually nondispersive) is given by

$$c_g \cong c_p \cong -\beta R_i^2 \propto \varphi^{-2} \tag{4}$$

[this relation is not valid in a zonal belt of few degrees around the equator, the equatorial β plane, where a discrete set of wave speeds exists—e.g., Gill (1982) and Philander (1990)]. For example, at $\varphi = 13°$N, $l = 2229$ km, in basic agreement with the offshore scale that can be estimated from Figs. 4, 5, and 6.

Observations of baroclinic Rossby wave phase speeds based on T/P data (Chelton and Schlax 1996) have revealed that, at midlatitudes, the linear nondispersive value (4) underestimates the real one by a factor 2 or more [see Killworth et al. (1997) for a theoretical analysis of this discrepancy and Zang and Wunsch (1999) for a critical overview]; however, for the intertropical latitudes considered in this analysis, observed and theoretical values are basically coincident. Observational evidence of beta-refraction patterns in the tropical North Pacific was first provided from an analysis of bathythermograph data by White (1977), and later, from T/P altimeter data by Chelton and Schlax (1996) and White et al. (1998). The observed patterns extend more westward than the ones produced by the present model, but this is due to the presence, in the real ocean, of waves with periods larger than the annual one (the only period considered here), such as the biennial or longer periods, with consequent larger offshore scale, according to the above discussion.

b. On the origin of Rossby waves emanating from the eastern boundary

Here we consider the origin of the westward propagating Rossby waves emanating from the eastern boundary discussed in the preceding section. It has been recognized in several studies, mainly devoted to analyzing El Niño events, that the eastern boundary of the ocean can be regarded as an extension of the equatorial wave guide (e.g., Anderson and Rowlands 1976; McCreary 1976; Clarke 1983; Johnson and O'Brien 1990; Shaffer et al. 1997; Soares et al. 1999). The arrival at the eastern boundary of an equatorial Kelvin wave generated in the equatorial region from changing winds leads to the reflection of a westward-propagating equatorial Rossby wave and to coastal Kelvin waves propagating poleward; in turn, this coastal signal acts as a boundary forcing for westward-propagating midlatitude Rossby waves.

For our study, we want to see if the same dynamical mechanism is also active in shaping the oceanic response to the seasonal forcing (3). In Fig. 7 *y*–*t* diagrams of the SSH (Fig. 7a) and interface displacement (Fig. 7b) along the eastern boundary (meridional section at $x = L$) are shown. It is evident that baroclinic coastal Kelvin waves are propagating away from the equator. Baroclinicity is implied by the fact that SSH and interface displacement are opposite in phase and with amplitudes whose ratio is $\approx\Delta\rho/\rho$; moreover, the poleward phase speed that can be evaluated from the isoline inclination is $c \approx 160$ km day^{-1}, in agreement with the theoretical value $c = \sqrt{g'\overline{D}} = 1.93$ m s^{-1}. The relation between the phase of the Kelvin wave at the equator and the wind forcing is crucial in the understanding of the overall dynamics and will be considered in section 5.

The generation of Rossby waves by the passage of Kelvin waves at the eastern boundary is elucidated in Fig. 8. The left-hand panel shows profiles of the SSH at the reference latitude $\varphi = 13°$N for four different instants of time covering a whole period, while the corresponding meridional profiles at the eastern boundary (from $\varphi = 13°$N southward) are shown in the right-hand panel, each signal pair being connected at $x = L$, $\varphi = 13°$N [in the small graph the whole meridional profiles including also the interval $\varphi = (13°\text{N}, 52°\text{N})$ are reported]. The profiles in the right-hand panel show northward-traveling coastal Kelvin waves while in the left-hand panel Rossby waves emanating from the eastern boundary are shown. The latter evidence westward phase propagation and a strong zonal modulation associated with the beta refraction.

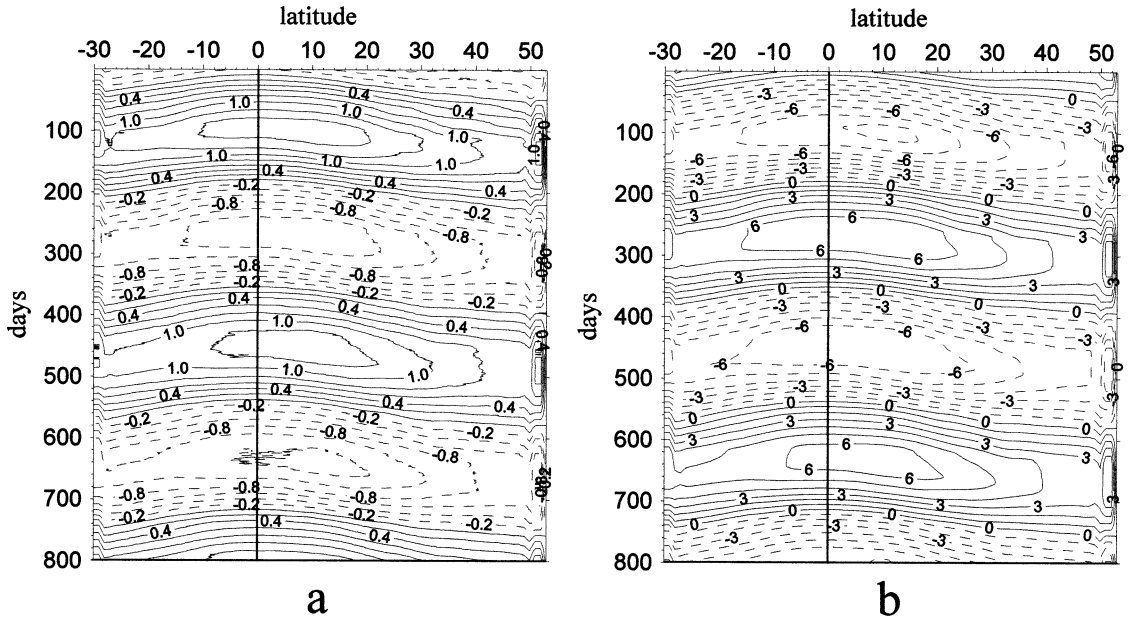

FIG. 7. (a) SSH y–t diagrams (cm) and (b) the interface displacement (m) along the eastern boundary (meridional section at $x = L$).

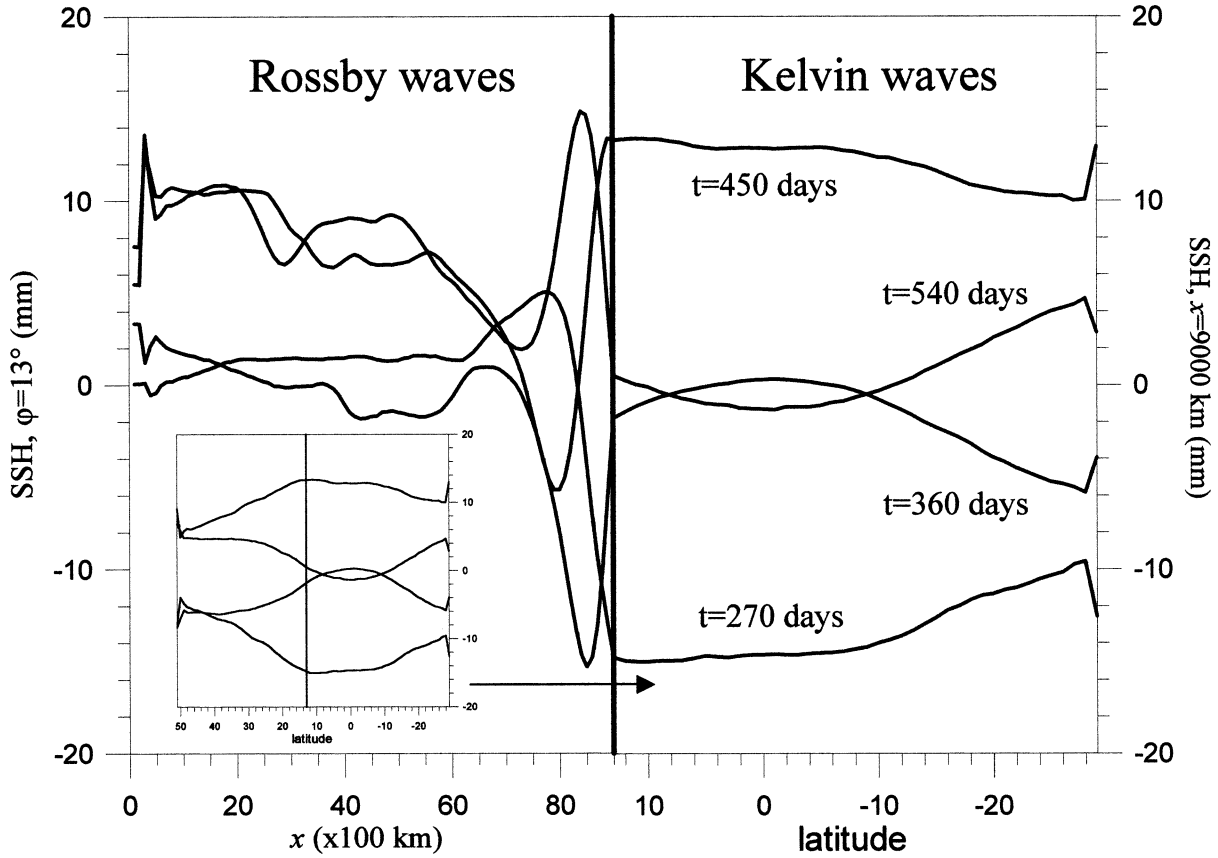

FIG. 8. (left) Zonal profiles of the SSH at $\varphi = 13°$N for four different instants of time of a whole cycle. (right) Meridional profiles of the SSH at the eastern boundary ($x = L$) from $\varphi = 13°$N southward for the same instants of time. Each signal pair is connected at $x = L$, $\varphi = 13°$N (vertical thick solid line). In the small graph the whole meridional profiles, including also the interval $\varphi = (13°\text{N}, 52°\text{N})$, are reported.

4. Validation with altimeter data

An idealized ocean model may allow for a more effective analysis of specific dynamical features than a state-of-the-art ocean general circulation model, but the significance of the conclusions is limited by the degree of realism of the idealized model; therefore, some validation of its results is essential. If the validation is successful one can then proceed to perform sensitivity experiments in order to shed light on particular aspects of the dynamics. The validation of model results will be performed in this section by comparing the latter with the analysis of Stammer (1997) based on T/P altimeter data. We will start by comparing zonal *x–t* diagrams, and then we will proceed to a quantitative comparison based on zonally integrated transport time series.

a. Comparison between numerical and T/P SSH x–t diagrams

Stammer (1997) obtained the global dynamically active signal (i.e., that related to subsurface geostrophic currents) using T/P data from repeat cycles 2–116 (October 1992–November 1995) after filtering out tidal, inverted barometer, and steric height signals. Diagrams showing SSH anomalies as a function of time were presented in Plate 3 of Stammer (1997), and the *x–t* diagrams of Fig. 4 are directly comparable with them. The initial time is roughly the same (8 October 1992 for T/P data and ≈15 October in our simulation); moreover, also the chosen aspect ratio is the same, so that the propagation speed of Rossby waves can be visually compared through the isoline inclination.

The agreement between our model results and T/P data can be considered as fairly good, since, despite the simplicity of the forcing and the oceanic model, the main features of the sea surface seasonal variability as observed by the satellite altimeter are captured by our model. At $\varphi = 5°$N annual Rossby waves are propagating westward (with the correct phase speed) over all longitudes, because no shadow zone is present at such low latitude (see Fig. 6a). There appears to be a time lag of ≈2 months between T/P data and model results for the first cycle, while also the phase is correct for the successive two cycles. Small-scale features at ~3000 km off the eastern boundary, present in T/P data and likely due to topographic effects, are obviously absent in model results because no variable topography is considered. At $\varphi = 10°$N, east of $x \sim 5500$ km, the waves are clearly radiating from the eastern boundary, and in this sector modeled and T/P annual Rossby waves compare very well. In the western sector Rossby waves appear to be originating at midbasin. In the model results we can suppose that open-ocean generation of Rossby waves by Ekman pumping is active (see section 5b). In real data we can again suppose that, apart from this, also topographic effects can contribute in western wave activity. At $\varphi = 25°$N modeled annual Rossby waves are again found to propagate with the correct phase and speed, and also the confinement is well reproduced. In the oceanic interior the model and data variabilities are, on the other hand, very different. The strong Rossby wave activity west of 200°E evident in T/P data and generated by topographic interactions cannot be produced by our flat-bottom ocean. Moreover, the barotropic westward-intensified seasonal fluctuations present in model results, and not evident in T/P data, could partly be hidden in the latter by the strong wave signal, and could also be overestimated in model results because the spatial structure of the wind forcing (Fig. 3) overestimates the wind stress curl in the western sector. At all latitudes the amplitude of the model variability is smaller than the data by about a factor of 2–3. This can be accounted for by the amplitude of the seasonally varying wind stress (3), which underestimates the real wind. In fact, as explained in section 2b, the wind stress was constructed from seasonal averages, with a consequent remarkable reduction of the effective variability.

In Stammer's (1997) paper the T/P data were also compared with numerical results obtained from the World Ocean Circulation Experiment (WOCE) Parallel Ocean Climate Model (Semtner and Chervin 1992) forced by daily ECMWF wind stress fields, and climatological seasonal surface T and S boundary conditions (Stammer et al. 1996). The agreement was remarkably good at various scales, and it was therefore noticed that global observations and numerical modeling have converged to a point that comparison of individual features present in ocean observations with simultaneous numerical simulations can be carried out. In view of this, what is the role of simplified models such as the present one? They can complement state-of-the-art models in providing explanation of specific dynamical processes through ad hoc sensitivity experiments. In fact, after having checked (as done in this section) that the dynamical aspects under investigation present in observed data are reproduced reasonably well by the model, then its simplified nature will allow one to perform modified runs that can highlight processes (see section 5) in a more convenient way than could be done with a highly realistic model.

b. Comparison between numerical and T/P zonally integrated transports

Let us now consider a validation based on zonally integrated transport time series. Stammer (1997) computed, from the dynamically active signal, meridional transport anomalies (that we denote as q_{ALT}, see below) through the geostrophic relation under the assumption of barotropic flow, and *integrated* meridional transport anomalies (that we denote as Q_{ALT}) by integrating q_{ALT} over three different zonal belts centered at $\varphi = 13°$, 31°, and 44°N, so as to get rid of small-scale features. The

belts covered all the longitudes, apart from a western sector (where westward intensified current fluctuations are expected), that was excluded from the integration. Comparison was then carried out between Q_{ALT} and the corresponding Sverdrup anomalies (that we denote as Q_{SVE}) obtained by performing the same spatial integration on meridional transports q_{SVE} computed from the ECMWF wind stress curl anomalies through the Sverdrup relationship. From this comparison at $\varphi = 13°$ it was found that Q_{ALT} and Q_{SVE} are highly correlated signals with an important seasonal component, and (a) the ratio μ between the Q_{SVE} rms and the Q_{ALT} rms is $\mu \approx 0.15$, and (b) Q_{SVE} leads Q_{ALT} with a time lag $\Delta\theta \approx 3$ months. The large discrepancy between Q_{ALT} and Q_{SVE} (which is much less pronounced or even disappears at higher latitudes) was ascribed to the failure of the assumption that the sea surface topography reflects barotropic transport fluctuations, since at this low latitude the ocean variability is mainly baroclinic. In the following we will construct quantities that correspond to those used by Stammer (1997), and will find good agreement with the parameters μ and $\Delta\theta$ obtained from T/P data.

From η_1 an *altimeter-equivalent* geostrophic meridional (volume) transport can be computed:

$$q_g = (D_1 + D_2)\frac{g}{f}\frac{\partial \eta_1}{\partial x}. \quad (5)$$

This transport corresponds to the one obtainable from the dynamically active altimeter-derived SSH under the assumption of barotropic flow. However, since comparison with the Sverdrup transport is looked for, we construct a corrected altimeter-equivalent meridional transport q_{ALT} that includes also the meridional Ekman transport $q_E = -(\boldsymbol{\tau})_x/\rho f$:

$$q_{ALT} = q_g + q_E. \quad (6)$$

By extending to the time-dependent case the classical stationary Sverdrup relationship (e.g., Pedlosky 1996), a meridional Sverdrup transport can be defined:

$$q_{SVE} = \frac{\mathrm{curl}_z \boldsymbol{\tau}}{\rho\beta}, \quad (7)$$

where $\boldsymbol{\tau}$ is given by (3). We then construct zonally integrated meridional (volume) transports as follows:

$$Q(\varphi, t) = \int_{x_0}^{L} dx' \int_{y(\varphi)-\Delta y}^{y(\varphi)+\Delta y} q(x', y', t)\, dy', \quad (8)$$

so that an integrated altimeter-equivalent meridional transport Q_{ALT} is obtained by substituting (6) into (8) and an integrated meridonal Sverdrup transport Q_{SVE} is obtained by substituting (7) into (8). The angle φ is the latitude at which the zonal belt is centered, and $y(\varphi)$ is the y coordinate corresponding to that latitude; moreover, Δy (which is chosen as 333 km, corresponding to 3° in latitude, in order to simulate Stammer's computations) is the semiwidth of the belt. The western extreme of the zonal belt is chosen as $x_0 = 1500$ km so that, as Stammer (1997) did, the western meridional belt where the Sverdrup relation is known a priori to fail is excluded from the integration. In general, both Q_{SVE} and Q_{ALT} yield very weak dependence on x_0, provided it is sufficiently large to exclude the region of westward-intensified current fluctuations, and sufficiently small not to approach the eastern boundary.

Figure 9a shows $Q_{ALT}(13°\mathrm{N}, t)$ (thick solid line) and $Q_{SVE}(13°\mathrm{N}, t)$ (dashed line). The ratio between the Q_{SVE} rms and the Q_{ALT} rms is $\mu \approx 0.12$, in good agreement with the corresponding value obtained from T/P data (which we recall is $\mu \approx 0.15$, as noticed at the beginning of this section). Moreover, also in these model results Q_{SVE} leads Q_{ALT}, as in T/P data, but with a time lag $\Delta\theta \approx 5$ months instead of $\Delta\theta \approx 3$ months. This difference of ≈2 months between observed and modeled $\Delta\theta$ can be explained as follows.

As we have already seen (section 3b) and we will see even more clearly in the next section, most of the baroclinic wind-driven response at extra-equatorial latitudes in the eastern sector of the ocean originates basically from wind changes in the equatorial region. In other words, Q_{ALT} (13°N, t) depends basically on wind activity at the equator rather than on the local winds. This, together with the verification (section 4a) that the SSH signal at different latitudes is substantially in phase with the observed T/P data allows us to conclude that the wind (3) is in phase with the real wind for near-equatorial latitudes, and that Q_{ALT} (13°N, t), as shown in Fig. 9a, is basically correct. On the other hand we observed (section 2b) that the ECMWF wind stress curl experiences a phase change of 4 months at $\varphi \approx 10°\mathrm{N}$ (Rienecker and Ehret 1988), while in our wind stress curl the phase change is 6 months. Thus, our wind (which has the correct phase for $\varphi < 10°\mathrm{N}$ as we have just seen) leads the real wind by $6 - 4 = 2$ months for $\varphi > 10°\mathrm{N}$. Such time shift does not affect the local response [and therefore $Q_{ALT}(13°\mathrm{N}, t)$], as noticed above, but it does produce a shifted Sverdrup transport Q_{SVE}, because this depends on the local wind stress curl. A *corrected* Sverdrup transport can be defined by shifting Q_{SVE} ahead by 2 months. In conclusion, the time lag between the corrected Q_{SVE} and Q_{ALT} would now be $\Delta\theta \approx 5 - 2 = 3$ months, in substantial agreement with T/P observations. Figure 9b shows the *shifted* $Q_{SVE}(13°\mathrm{N}, t)$ (dashed line) and $Q_{ALT}(13°\mathrm{N}, t)$ scaled by the factor $\mu \approx 0.12$ (solid line): this figure is directly comparable with Stammer's (1997) Fig. 5c. The gross features of the fluctuations are indeed captured by our simple model.

One last comment concerns the validity of the time-dependent Sverdrup balance. The large departure between the Sverdrup transport and the transport obtained from the SSH fluctuations under the assumption of barotropic flow observed in both T/P data and model results does not imply that the Sverdrup balance does not hold, but simply that the flow has a predominant baroclinic

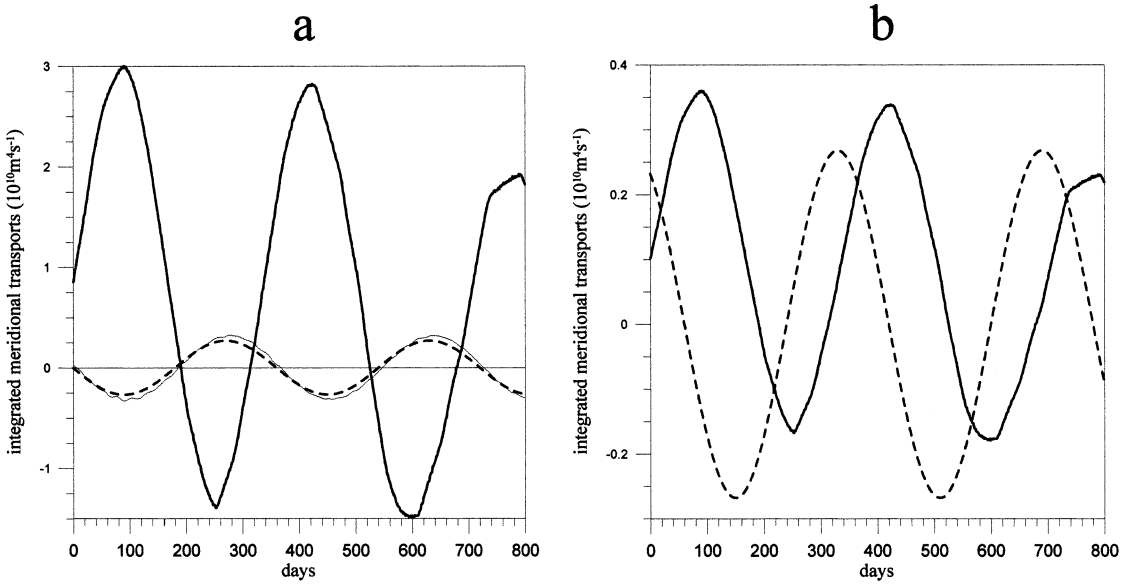

FIG. 9. (a) Thick solid line: Q_{ALT}(13°N, t); dashed line: Q_{SVE}(13°N, t); thin solid line: Q_{NET}(13°N, t) (see text). (b): Solid line: Q_{ALT}(13°N, t) scaled through the factor $\mu \approx 0.12$; dashed line: shifted (see text) Q_{SVE}(13°N, t). Panel (b) is directly comparable with Stammer's (1997) Fig. 5c.

component. In fact, in the absence of topographic effects the Sverdrup balance is expected to hold in the oceanic interior even if the flow is baroclinic (e.g., Pedlosky 1996), and the same can be said for the *time-dependent Sverdrup balance* for sufficiently long forcing periods, such as the annual one (Willebrand et al. 1980; Pierini 1998). In this context such balance is expressed by the relation

$$Q_{SVE} \approx Q_{NET}, \tag{9}$$

where Q_{NET} is obtained by applying (8) to the vertically integrated model transport:

$$q_{NET} = H_1 v_1 + H_2 v_2.$$

Figure 9a (where Q_{NET} is given by the thin solid line) shows that the time-dependent Sverdrup balance (9) actually holds, as expected (the small departure between the two signals is due to weak inertial effects associated with the seasonal variability). The local effect of the wind at this latitude is only a small barotropic residual, which is superimposed on a much larger baroclinic Rossby wave signal of remote origin. On the contrary, at midlatitudes one would have a wind-driven barotropic flow for which $Q_{SVE} \approx Q_{NET} \approx Q_{ALT}$, as confirmed by the analysis (not shown) of these transports at extratropical latitudes. Similar conclusions based on T/P data were drawn by Vivier et al. (1999) who found that the (nonzonally integrated) small barotropic annual residual is, more precisely, in ''topographic Sverdrup balance'' (e.g., Niiler and Koblinsky 1985). Our results are also in agreement with those of Vivier et al. (1999) and Fu and Davidson (1995) in recognizing that the time-dependent Sverdrup balance response is predominant over the Rossby wave signal only for latitudes higher than $\approx 40°$.

5. Sensitivity experiments

In section 3 we saw that the modeled wind-driven seasonal variability in the tropical North Pacific outside the equatorial band is basically in the form of annual beta-refracted baroclinic Rossby waves freely propagating away from the eastern boundary. We considered in particular the origin of such waves (section 3b) and concluded that they are generated by the passage of northward propagating coastal Kelvin waves, which are in turn originating from the equatorial region. Thus, this dynamical mechanism known to act in El Niño events appears to play a major role also in shaping the seasonal variability.

It should be noticed, however, that the observed annual Rossby waves radiating from the eastern boundary of the ocean are, in several studies, considered to be *locally* generated by the wind field. Stammer (1997) regarded the westward propagating SSH anomalies at 10°N shown in a T/P x–t diagram (our Fig. 4 is a model counterpart) as being generated locally off the eastern boundary by the wind field during specific seasons. White (1977), Meyers (1979), White and Saur (1981), and Cummins et al. (1986) all considered similar local mechanisms to be the origin of such waves in the North Pacific, and Krauss and Wuebber (1982) and Herrmann and Krauss (1989) performed analogous studies and drew analogous conclusions for the North Atlantic.

On the other hand, several observational and theoretical studies support the alternative generation mech-

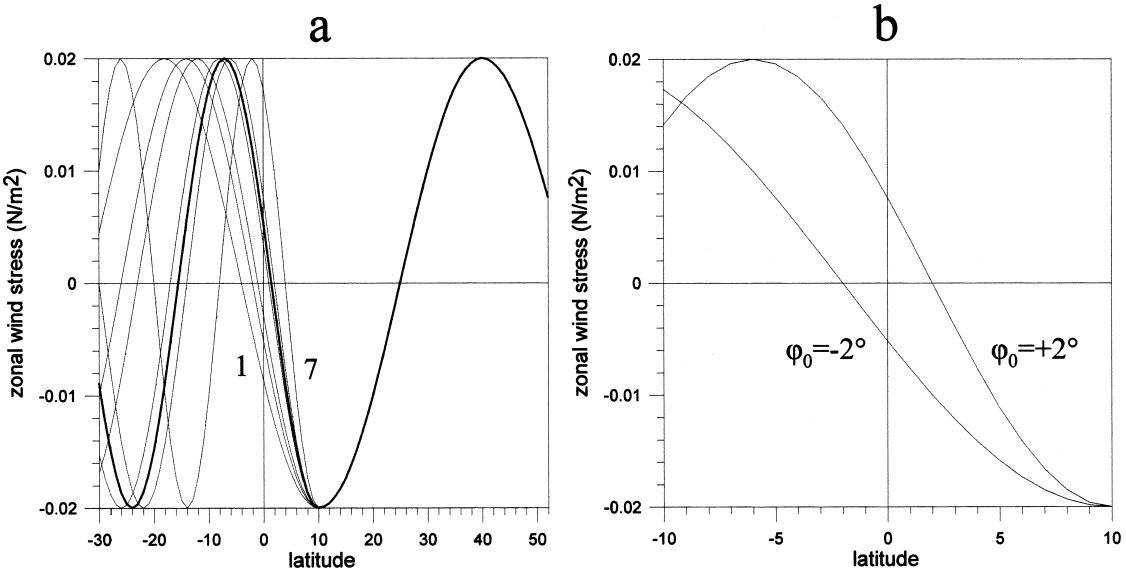

FIG. 10. (a) Lines 1–7: amplitudes of the seasonally varying zonal wind stress forcing at $x = 4500$ km for $\varphi_0 = -4°$, $-2°$, $-1°$, $1°$, $1.5°$, $2°$, and $4°$, respectively (see text). (b) Zooming of wind profiles for $\varphi_0 = \pm 2°$.

anism that came out in the present model study, for which annual Rossby waves are mainly remotely forced at the equator. Vivier et al. (1999) recognized from T/P data that, while near-annual period Rossby waves in the western Pacific are correlated with the wind stress curl, in the eastern Pacific they are rather correlated with SSH anomalies at the equator. Qiu et al. (1997) and Soares et al. (1999) present modeling results in which annual forcing at the equator produces annual Rossby waves at the eastern boundary through the mechanism described above.

Thus, while it is clear that both local and equatorial wind forcings are able to radiate annual Rossby waves from the eastern boundary of the tropical North Pacific, in the present model study the result has emerged that T/P data are compatible with a mainly remote equatorial forcing. In this section sensitivity experiments will be presented aimed at providing further evidence of this dynamical behavior and obtaining a deeper insight into its functioning. Sensitivity experiments (not shown), in which small modifications of the wind forcing and of the geometry of the basin (including an inclined eastern boundary) were introduced, showed that the oceanic response described in section 3 is very robust, since it yielded relative deviations comparable to those introduced, but with one important exception that we are now going to discuss.

a. Effect of phase variations of the zonal winds in the equatorial band

Let us define φ_0 as the latitude at which the zonal wind stress in the middle of the basin ($x = 4500$ km) vanishes: Fig. 2 shows that our wind forcing (thin dashed line) corresponds to the value $\varphi_0 = 1.5°$. Then, let us consider wind forcings that differ from the basic one for small variations of φ_0 (the zonal structure shown in Fig. 3a remaining unchanged). In Fig. 10a seven different profiles are reported corresponding to the values $\varphi_0 = -4°$, $-2°$, $-1°$, $1°$, $1.5°$, $2°$, and $4°$. For latitudes $\varphi > 10°$N all these wind systems are exactly equal to the basic one of section 3, and only for latitudes south of $\varphi \sim 10°$S is the wind very different from the latter (but the southern sector of the basin has no relevance in determining the response north of the equator). Therefore one might expect in principle the various oceanic responses in the northern sector to yield only minor differences with respect to the basic one. On the contrary, the analysis of the responses shows that this is not the case. Figure 11 shows zonal profiles of the SSH at $t = 540$ days at three different latitudes ($\varphi = 6°$, $13°$, $20°$N) for the seven different wind systems. Let us consider, for instance, the cases $\varphi_0 = -2°$ and $\varphi_0 = +2°$ (Fig. 10b): despite the small difference in the forcing structure, the two responses are almost opposite in phase! It can also be noticed that for different negative values of φ_0 the phase is almost identical, and the same holds for positive values of φ_0. In all cases the amplitude of the response increases for increasing $|\varphi_0|$.

This apparently paradoxical behavior can be explained as follows. The cases $\varphi_0 = -2°$ and $\varphi_0 = +2°$ (chosen for reference) have winds opposite in phase in a narrow band centered at the equator, and this produces the difference in the response according to the mechanism delineated in section 3b. For instance, in the case $\varphi_0 = +2°$, when the wind is positive—that is, eastward [for $0 < \omega t < \pi$ in (3), which corresponds roughly to autumn and winter]—piling up of water along the equator displaces the SSH upward and the interface downward with a consequent production of an equatorial

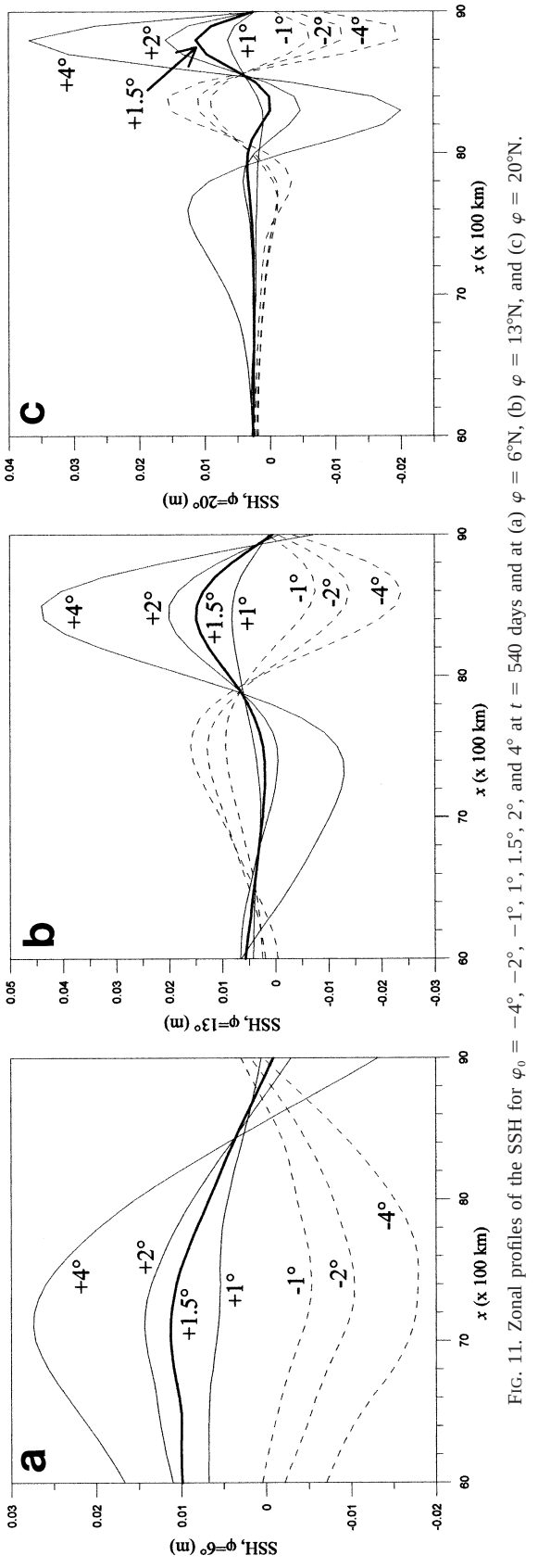

FIG. 11. Zonal profiles of the SSH for $\varphi_0 = -4°$, $-2°$, $-1°$, $1°$, $1.5°$, $2°$, and $4°$ at $t = 540$ days and at (a) $\varphi = 6°$N, (b) $\varphi = 13°$N, and (c) $\varphi = 20°$N.

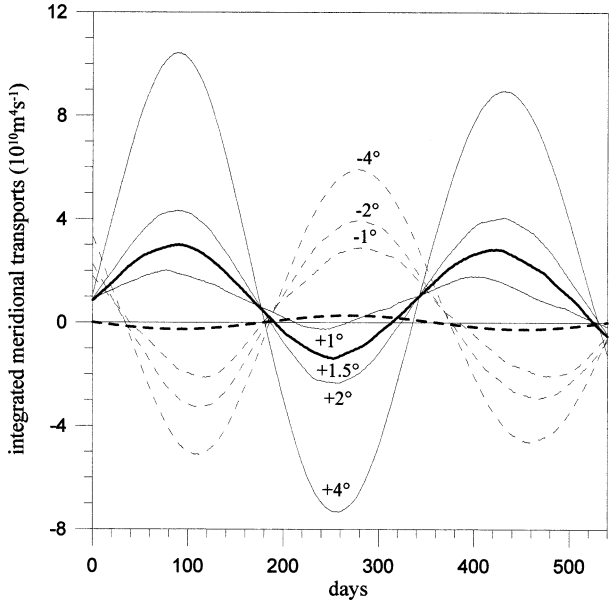

FIG. 12. Solid and thin dashed lines: $Q_{ALT}(13°N, t)$ for $\varphi_0 = -4°$, $-2°$, $-1°$, $1°$, $1.5°$, $2°$, and $4°$. Thick dashed line: $Q_{SVE}(13°N, t)$ (independent of φ_0).

Kelvin wave that will soon transfer this information along the eastern coast through propagation of coastal Kelvin waves. No appreciable time lag between this downwelling phase along the equator and the corresponding one along the coast in the vicinity of the equator is expected because of the existence of zonal winds up to the eastern boundary (Fig. 3a). This synchronization between the equatorial zonal wind and upwelling/downwelling near the eastern boundary can be checked from the y–t diagrams of Fig. 7 taking into account the phase of the zonal wind given by (3). Now, during the same half period ($0 < \omega t < \pi$), in the case $\varphi_0 = -2°$ the zonal wind near the equator will be negative, that is, westward; therefore the considerations made above lead to the conclusion that in this case the response must be almost opposite in phase with respect to that for $\varphi_0 = +2°$, as shown by Fig. 11. It should be noticed that the zonal winds in the two cases are not symmetric relative to the equator (Fig. 10b), and this explains the not exactly 180° phase lag between the two cases. Moreover, the larger $|\varphi_0|$ is, the larger the winds around the equator are, and this explains the increasing amplitude of the response for increasing $|\varphi_0|$.

Figures 12 and 13 show how the parameters introduced in section 4b for quantitative validation with Stammer's (1997) altimeter data are modified for different values of φ_0. Figure 12 shows $Q_{ALT}(13°N, t)$ for the seven different values of φ_0, including the one ($\varphi_0 = 1.5°$, thick solid line) that corresponds to our basic experiment (already shown in Fig. 9a), along with $Q_{SVE}(13°N, t)$ (thick dashed line), which is independent of φ_0. The lines show differences analogous to those discussed in connection to SSH zonal sections (Fig. 11).

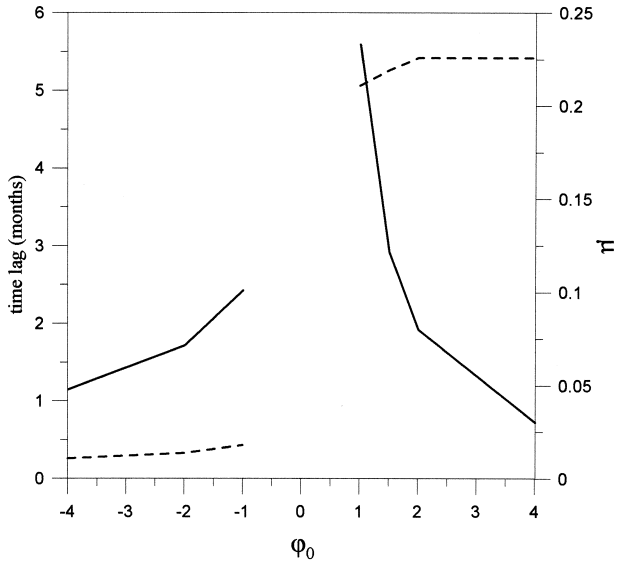

FIG. 13. Dashed line: time lag between $Q_{ALT}(13°N, t)$ and the nonshifted $Q_{SVE}(13°N, t)$ as a function of φ_0. Solid line: ratio μ between the $Q_{SVE}(13°N, t)$ rms and the $Q_{ALT}(13°N, t)$ rms as a function of φ_0.

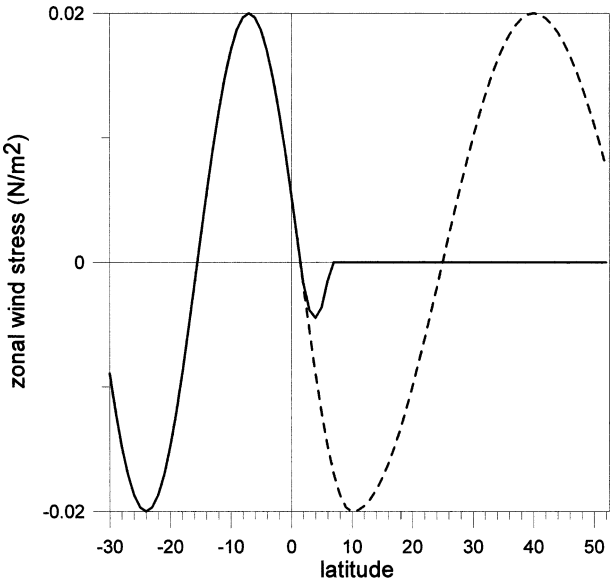

FIG. 14. Dashed line: amplitude of the seasonally varying zonal wind stress forcing used in the basic numerical experiment at $x = 4500$ km. Solid line: Profile of the *confined* forcing used in the numerical experiment described in section 5b.

In Fig. 13 μ and (the nonshifted value of) $\Delta\theta$ are shown as a function of φ_0 (in the gap $-1° < \varphi_0 < +1°$ no values are reported because, owing to the particular structure of the Q_{ALT} profiles, no phase difference $\Delta\theta$ can be defined). The interesting information summarized in Fig. 13 is that both μ and $\Delta\theta$ are highly sensitive to the structure of the zonal wind field in the equatorial band, and this makes the validation with altimeter data performed in section 4 particularly significant. In fact, small differences of φ_0 from its correct value $\approx 1.5°$ (see thick dashed line of Fig. 2) would make the validation fail dramatically.

b. *Response to a zonal wind system confined in the equatorial band*

The sensitivity experiments of section 5a confirm that, as already evidenced in section 3, the wind-driven oceanic response in the tropical Pacific is determined near the equator, and show that the equatorial band within which the signal is originated extends only very few degrees around the equator, since a change of φ_0 of just 2°–4° is sufficient to produce a phase shift in the tropical response of ~180° (~6 months). This is further evidence that the seasonal variability behaves like a kind of ''periodic'' El Niño, since McCreary (1976) already found that only winds within an equatorial band of ±5° of latitude are important in generating an El Niño event. In order to put in evidence this behavior in a drastic way we now use a forcing with the same zonal structure as that shown in Fig. 3a, but whose profile at $x = 4500$ km is shown in Fig. 14 (solid line), as compared with that of the basic experiment (dashed line). The zonal winds are equal to those of the basic experiment up to $\varphi \sim 2.5°$N and vanish at $\varphi \sim 7°$N. The dependence of the response in the tropical Pacific on the equatorial winds suggests that this confined wind system should produce a response similar to that discussed in section 3. This is indeed the case, as shown in the SSH x–t diagrams of Fig. 15, that correspond to those of Fig. 4.

The SSH signal at 5°N is virtually equal to that of Fig. 4, apart from a small time lag. At 10°N we noticed in section 4a that the response to the realistic forcing shows two distinctive aspects: east of $x \sim 5500$ km Rossby waves radiating from the eastern boundary are present, while in the central and western part of the basin there are Rossby waves, which appear to be originating in the open ocean, and which we supposed being generated via the mechanism of Ekman pumping. The x–t diagram at $\varphi = 10°$N of Fig. 15 shows that the Rossby waves originating from the eastern boundary are present also now and with the same characteristics (in agreement with the remote generating mechanism), while those in the western sector are absent, and this is clearly due to the absence of wind at $\varphi > 7°$N. Consequently we have confirmation that the Rossby waves found in the northwestern tropical Pacific when realistic forcing is used are generated at midbasin by Ekman pumping. Rossby waves are indeed known to be excited in the Pacific midbasin by a local Ekman pumping response coherent with the wind stress curl, as reported by Meyers (1979), Kessler (1990), and Vivier et al. (1999). At 25°N the Rossby waves near the eastern boundary for the realistic and confined wind forcing are virtually coincident, while the barotropic westward intensified oscillations generated by the realistic forcing are obviously absent when the confined forcing is used.

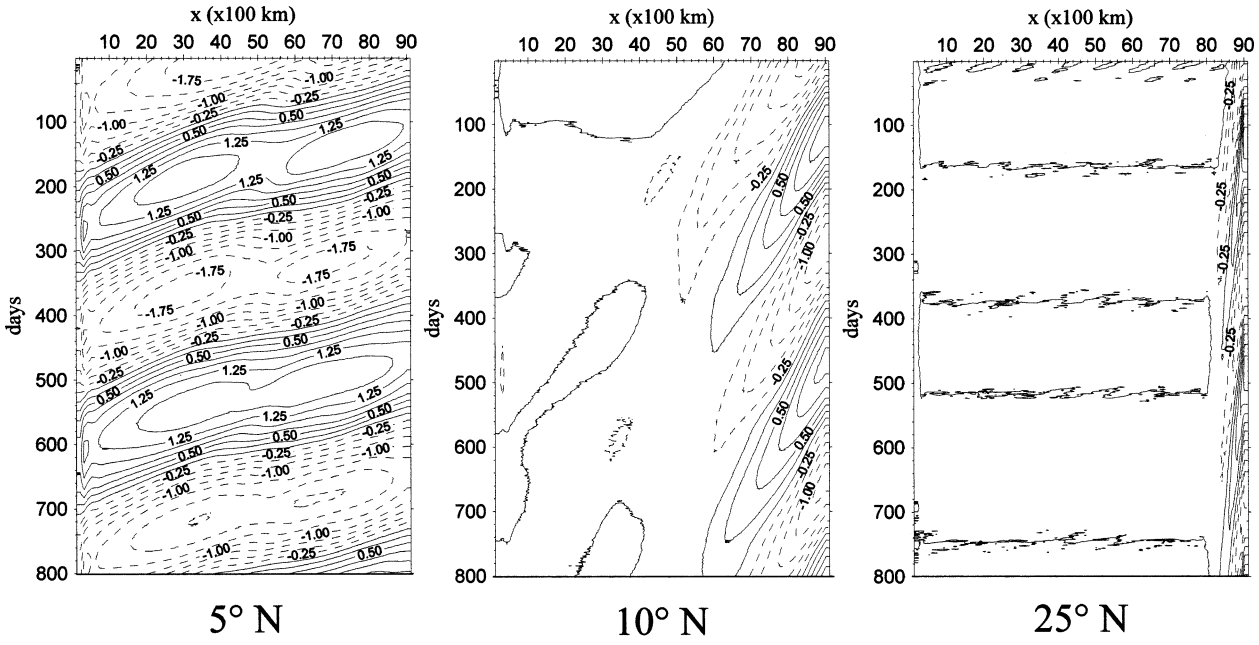

FIG. 15. SSH *x–t* diagrams at $\varphi = 5°$, 10°, and 25°N produced by the *confined* wind forcing (amplitudes: cm).

6. Conclusions

In this paper the wind-driven seasonal variability in the tropical North Pacific was analyzed through a process study, in which the idealized model setup (a two-layer primitive equation ocean model in a flat rectangular ocean) is accompanied by an idealized seasonally varying wind forcing obtained from realistic wind data (ECMWF seasonal climatology). The oceanic response in the eastern tropical region is found to be mainly in the form of annual beta-refracted baroclinic Rossby waves radiating from the eastern boundary, in agreement with in situ measurements and recent remote sensing information. A quantitative validation of these model results with those of Stammer (1997) based on TOPEX/Poseidon (T/P) altimeter data was then carried out. The comparison between modeled and T/P sea surface height anomalies along zonal sections at three different tropical latitudes shows that, despite its simplicity, the model is able to reproduce with sufficient accuracy the main features and phase of the seasonal variability in the eastern tropical North Pacific. Moreover, a further validation was performed by means of zonally integrated meridional transports computed from the SSH under the assumption of barotropic flow and from the winds through the Sverdrup relation, and, again, good agreement is found.

An interesting information obtained from a detailed analysis of the results and from ad hoc sensitivity experiments concerns the mechanism through which the seasonal variability in the eastern tropical North Pacific is generated. The annual beta-refracted baroclinic Rossby waves radiating from the eastern boundary are found to be generated by the passage of northward-propagating coastal Kelvin waves, which are in turn originating from the equatorial region. This is the same dynamical mechanism known to play a major role in the dynamics of El Niño events, which thus appears to be active also in shaping the oceanic response to seasonally varying winds (but is expected to be a fundamental aspect of the wind-driven variability also on longer timescales).

An apparently paradoxical consequence of this dynamical behavior lies in the dependence of the wind-driven seasonal signal over a vast area of the tropical ocean (even far away from the eastern boundary) on winds in a very narrow equatorial band rather than on the local wind stress curl, as it could be expected if ageostrophic boundary effects were absent. In a sensitivity experiment (section 5a) it was shown, among the other things, that what establishes the phase of the seasonal variability in the eastern (and partly in the central) part of the ocean for $\varphi = 0° \sim 30°$ is not the wind over this band but that at $\sim 2°\text{S} < \varphi < \sim 2°\text{N}$. Another sensitivity experiment (section 5b) shows that, obviously, the local wind stress curl at $\varphi = 0° \sim 30°$ does produce a local Ekman pumping response, and consequent open ocean generation of Rossby waves, but this signal is overwhelmed (particularly in the eastern Pacific) by the stronger remotely generated annual Rossby wave field. These results also include information on the response to interannual wind anomalies superimposed on the seasonal variability. A remarkable relaxation of the trade winds around the equator in an El Niño year implies strong westerly wind anomalies and consequent downwelling at the eastern tropical boundary: in winter this is an amplification of the usual seasonal cycle as modeled in section 3 (in a ''La Niña,'' on the other hand,

the wind anomaly is reversed with respect to the seasonal signal since the trade winds intensify).

A technical conclusion can also be drawn from this model study, concerning the essential features that must be included in a model in order to obtain a realistic wind-driven seasonal (or longer period) variability. Apart from ocean general circulation models (which, naturally, include all the effects needed), simplified models aimed at performing process-oriented studies must include the equatorial region in the model domain (otherwise the remote equatorial forcing of Rossby waves is absent) and, moreover, must not be quasigeostrophic (otherwise the ageostrophic teleconnection provided by the Kelvin waves is filtered out). For example, in the model studies of Cummins et al. (1986) and Herrmann and Krauss (1989) the remote generating mechanism found in the present study is absent because they considered domains that extended only north of 15° and 10°N, respectively. Even if they had included the equatorial band they still would not have obtained the remote Rossby wave forcing, however, because they used quasigeostrophic equations.

One last comment concerns the possibility of extending the model in order to include relatively realistic topography and mean flows. The Pacific Ocean does not present a strong and extensive topographic feature such as the Atlantic midocean ridge, but nonetheless the inclusion of topography would certainly increase the degree of realism of the model (particularly in the central and western sectors). In addition, mean currents (the subtropical gyre, the North Equatorial Current and Countercurrent and Equatorial Undercurrent) should be produced by a wind field that include also an appropriate time-independent component (e.g., the mean zonal winds represented by the thick solid line of Fig. 2). Mean currents would Doppler shift the waves, but in the tropical band the Rossby wave speed is so high that this effect is not expected to be very relevant (otherwise the good comparison of our model with T/P data could not be realized). The zonal inclination of the interface associated with mean currents would, on the other hand, introduce a variation of Rossby wave speed with longitude. Nonlinear interactions could arise as well but, again, the successful validation of this idealized model suggests that all possible improvements would not be likely to produce fundamental modifications on the specific aspects dealt with here.

Acknowledgments. This research was supported by ASI, the Italian Space Agency.

REFERENCES

Anderson, D. L. T., and P. W. Rowlands, 1976: The role of inertia-gravity and planetary waves in the response of a tropical ocean to the incidence of an equatorial Kelvin wave on a meridional boundary. *J. Mar. Res.*, **34,** 295–312.

Chelton, D. B., and M. G. Schlax, 1996: Global observations of oceanic Rossby waves. *Science,* **272,** 234–238.

Clarke, A. J., 1983: The reflection of equatorial waves from oceanic boundaries. *J. Phys. Oceanogr.,* **13,** 1193–1207.

Cummins, P. F., L. A. Mysak, and K. Hamilton, 1986: Generation of annual Rossby waves in the North Pacific by the wind stress curl. *J. Phys. Oceanogr.,* **16,** 1179–1189.

Fu, L. L., and R. A. Davidson, 1995: A note on the barotropic response of sea level to time-dependent wind forcing. *J. Geophys. Res.,* **100,** 24 955–24 963.

——, and A. Cazenave, 2001: *Satellite Altimetry and Earth Sciences.* Academic Press, 480 pp.

——, and D. B. Chelton, 2001: Large-scale ocean circulation. *Satellite Altimetry and Earth Sciences,* L. L. Fu and A. Cazenave, Eds., Academic Press, 133–169.

Gill, A. E., 1982: *Atmosphere–Ocean Dynamics.* Academic Press, 662 pp.

——, and P. P. Niiler, 1973: The theory of the seasonal variability in the ocean. *Deep-Sea Res.,* **20,** 141–177.

Herrmann, P., and W. Krauss, 1989: Generation and propagation of annual Rossby waves in the North Atlantic. *J. Phys. Oceanogr.,* **19,** 727–744.

Isoguchi, O., H. Kawamura, and T. Kono, 1997: A study on wind-driven circulation in the subarctic North Pacific using TOPEX/Poseidon altimeter data. *J. Geophys. Res.,* **102,** 12 457–12 468.

Johnson, M. A., and J. J. O'Brien, 1990: The role of coastal Kelvin waves on the northeast Pacific Ocean. *J. Mar. Syst.,* **1,** 29–38.

Kessler, W. S., 1990: Observations of long Rossby waves in the northern tropical Pacific. *J. Geophys. Res.,* **95,** 5183–5217.

Killworth, P. D., D. B. Chelton, and R. A. De Szoeke, 1997: The speed of observed and theoretical long extratropical planetary waves. *J. Phys. Oceanogr.,* **27,** 1946–1966.

Krauss, W., and C. Wuebber, 1982: Response of the North Atlantic to annual wind variations along the eastern coast. *Deep-Sea Res.,* **29,** 851–868.

McCreary, J., 1976: Eastern tropical ocean response to changing wind systems: With application to El Niño. *J. Phys. Oceanogr.,* **6,** 632–645.

Meyers, G., 1979: On the annual Rossby wave in the tropical North Pacific Ocean. *J. Phys. Oceanogr.,* **9,** 663–674.

Niiler, P. P., and C. J. Koblinsky, 1985: A local time dependent Sverdrup balance in the eastern North Pacific Ocean. *Science,* **229,** 754–756.

Pedlosky, J., 1996: *Ocean Circulation Theory.* Springer, 453 pp.

Philander, S. G., 1990: *El Niño, La Niña, and the Southern Oscillation.* Academic Press, 289 pp.

——, and J. H. Yoon, 1982: Eastern boundary currents and coastal upwelling. *J. Phys. Oceanogr.,* **12,** 862–879.

Picaut, J., and A. J. Busalacchi, 2001: Tropical ocean variability. *Satellite Altimetry and Earth Sciences,* L. L. Fu and A. Cazenave, Eds., Academic Press, 217–236.

Pierini, S., 1996: Topographic Rossby modes in the Strait of Sicily. *J. Geophys. Res.,* **101,** 6429–6440.

——, 1998: Wind-driven fluctuating western boundary currents. *J. Phys. Oceanogr.,* **28,** 2185–2198.

Qiu, B., W. Miao, and P. Müller, 1997: Propagation and decay of forced and free baroclinic Rossby waves in off-equatorial oceans. *J. Phys. Oceanogr.,* **27,** 2405–2417.

Rienecker, M. M., and L. L. Ehret, 1988: Wind stress curl variability over the North Pacific from the Comprehensive Ocean–Atmosphere Data Set. *J. Geophys. Res.,* **93,** 5069–5077.

——, R. Atlas, S. D. Schubert, and C. S. Willet, 1996: A comparison of surface wind products over the North Pacific Ocean. *J. Geophys. Res.,* **101,** 1011–1023.

Robinson, I. S., 1994: *Satellite Oceanography.* Wiley, 455 pp.

Schopf, P. S., D. L. T. Anderson, and R. Smith, 1981: Beta-dispersion of low-frequency Rossby waves. *Dyn. Atmos. Oceans,* **5,** 187–214.

Semtner, A. J., and R. M. Chervin, 1992: Ocean general circulation from a global eddy-resolving model. *J. Geophys. Res.,* **97,** 5493–5550.

Shaffer, G., O. Pizarro, L. Djurfeldt, S. Salinas, and J. Rutllant, 1997: Circulation and low-frequency variability near the Chilean coast:

remotely forced fluctuations during the 1991–92 El Niño. *J. Phys. Oceanogr.,* **27,** 217–235.

Soares, J., I. Wainer, and N. C. Wells, 1999: Reflection of equatorial Kelvin waves at eastern ocean boundaries. Part I: Hypothetical boundaries. *Ann. Geophys.*, **17,** 812–826.

Stammer, D., 1997: Steric and wind-induced changes in TOPEX/POSEIDON large-scale sea surface topography observations. *J. Geophys. Res.*, **102,** 20 987–21 009.

——, R. Tokmakian, A. Semtner, and C. Wunsch, 1996: How well does a 1/4° global circulation model simulate large-scale oceanic observations? *J. Geophys. Res.,* **101,** 25 779–25 812.

Vivier, F., K. A. Kelly, and L. A. Thompson, 1999: Contributions of wind forcing, waves, and surface heating to sea surface height observations in the Pacific Ocean. *J. Geophys. Res.,* **104,** 20 767–20 788.

White, W. B., 1977: Annual forcing of baroclinic long waves in the tropical North Pacific Ocean. *J. Phys. Oceanogr.,* **7,** 50–61.

——, and J. F. T. Saur, 1981: A source of annual baroclinic waves in the eastern subtropical North Pacific. *J. Phys. Oceanogr.,* **11,** 1452–1462.

——, Y. Chao, and C. K. Tai, 1998: Coupling of biennial oceanic Rossby waves with the overlying atmosphere in the Pacific basin. *J. Phys. Oceanogr.,* **28,** 1236–1251.

Willebrand, J., S. G. H. Philander, and R. C. Pacanowski, 1980: The oceanic response to large-scale atmospheric disturbances. *J. Phys. Oceanogr.,* **10,** 411–429.

Zang, X., and C. Wunsch, 1999: The observed dispersion relationship for North Pacific Rossby wave motions. *J. Phys. Oceanogr.,* **29,** 2183–2190.